symmetry

MDPI

Article

Local-Energy-Conservation-Based Decomposition Method for Wall Friction and Heat Flux

Mingzhi Tang [1,2], Wenfeng Zhou [1,2], Yanchao Hu [1,2,*], Gang Wang [1,2] and Yanguang Yang [2,3,*]

[1] Hypervelocity Aerodynamics Institute, China Aerodynamics Research and Development Center, Mianyang 621000, China; tangmingzhi@cardc.cn (M.T.); zhouwenfeng@cardc.cn (W.Z.); wanggang@cardc.cn (G.W.)
[2] National Key Laboratory of Aerospace Physics in Fluids, Mianyang 621000, China
[3] China Aerodynamics Research and Development Center, Mianyang 621000, China
* Correspondence: huyanchao@cardc.cn (Y.H.); yangyanguang@cardc.cn (Y.Y.)

Abstract: A novel decomposition method that adheres to both local time translation symmetry and spatial rotational symmetry is proposed in this study, thereby extending the limitations of existing methods, which are typically restricted to quasi-two-dimensional configurations. Grounded in the FIK and RD identities, this method provides a clear physical and reliable interpretation suitable for arbitrary-curvature profiles. Utilizing this method, an analysis of the aerothermodynamic characteristics of the bistable states of curved compression ramp flows was conducted. The results reveal that the generation of undisturbed and peak C_f is dominated by viscous dissipation. Specifically, flow separation happens when all of the energy input from the work exerted by the adverse pressure gradient (APG) is insufficient to be entirely converted into local viscous dissipation and kinetic energy. Furthermore, the propensity for flow separation at higher wall temperatures is firstly elucidated quantitatively from the perspective of the work by the APG. The peak heat flux is predominantly triggered by the work of viscous stress, with the secondary contribution from energy transport playing a more significant role in the generation of the peak heat flux of the separation state than that of the attachment state.

Keywords: time translation symmetry; decomposition method; generation mechanism; wall friction; heat flux

check for updates

Citation: Tang, M.; Zhou, W.; Hu, Y.; Wang, G.; Yang, Y. Local-Energy-Conservation-Based Decomposition Method for Wall Friction and Heat Flux. *Symmetry* **2024**, *16*, 1147. https://doi.org/10.3390/sym16091147

Academic Editors: Calogero Vetro and Constantin Fetecau

Received: 28 May 2024
Revised: 7 August 2024
Accepted: 9 August 2024
Published: 4 September 2024

Copyright: © 2024 by the authors. Licensee MDPI, Basel, Switzerland. This article is an open access article distributed under the terms and conditions of the Creative Commons Attribution (CC BY) license (https://creativecommons.org/licenses/by/4.0/).

1. Introduction

Shock-wave/boundary-layer interaction (SBLI) frequently occurs on the deflected control surface of a vehicle during its supersonic/hypersonic flight. SBLI may cause significant flow separation and severe peak heat flux, resulting in a substantial reduction in control effectiveness and even a loss of control [1–4]. During flight, wall friction can contribute as much as 50 percent to the total drag [5], and the peak heat flux induced by SBLI and shock/shock interactions (SSIs) can reach 10 $\sim$ 100 times that without interactions [6]. Therefore, clarifying the generation mechanism of wall friction and peak heat flux is essential for further control intention.

To elucidate the individual contributions of different physical processes to the frictional drag for further guidance on wall friction control, Fukagata, Iwamoto and Kasagi [7] proposed a relationship (referred to as the FIK identity) by integrating the momentum equation. The FIK identity provides a quantitative analysis method for researchers to understand the generation and control mechanisms of wall friction and has been widely applied. By generalizing the FIK identity to compressible flows, Gomez et al. [8] analyzed the compressibility impact on the generation of mean wall friction drag, but their analysis did not quite focus on the impact of compressibility on the contribution terms. However, the FIK identity is generally thought to lack a simple physical interpretation involved in the derivation. Therefore, Renard and Deck [9] proposed a decomposition method (called the

RD identity) based on the Galileo transform and streamwise kinetic energy equation, which has a clearer physical interpretation. This method was extended to compressible flows by Li et al. [10]. Combined with empirical mode decomposition or spectral form equations, the FIK and RD identities help researchers investigate the roles of different flow structures in the generation of wall friction [11–13]. Another obvious benefit of decomposition methods is that they clarify the direction of each part of the energy [14–16], which is helpful in exploring a more efficient flow control method.

The accurate prediction of heat flux is very important for the thermal protection design of high-speed vehicles, and there exist some classical pressure–heat flux scaling relations [1,2,17–20]. However, the generation mechanism of heat flux is still vague. To understand this mechanism, the FIK and RD identities have also been extended to heat flux decomposition, such as in the studies by Zhang and Xia [21,22] and Sun et al. [23]. The heat flux decomposition method was also further derived to investigate the heat flux generation mechanism of turbulent flows in a high-enthalpy scenario by Li et al. [24]. In addition, Zhang and Xia [22] analyzed the results of different forms of heat flux decomposition by the FIK and RD identities and concluded that the twofold repeated integration of the FIK identity had a better physical interpretation. And Wenzel, Gibis and Kloker [25] hold the same viewpoint. However, they did not provide the physical image. In fact, some arbitrariness still exists in the selection of the order of integrals in the FIK identity or the transformation speed in the RD identity. In addition, different understandings of the physical processes of the contributions in the FIK and RD identities also lead to significant differences in understanding the influence of different contributions [26].

The present decomposition analyses mainly focus on the equilibrium flow in quasi-two-dimensional flows, such as channel flow and flat-plate flow. Sagaut and Peet [27] and Bannier, Garnier and Sagaut [28] extended the FIK identity to surfaces with spanwise complex geometries like riblets, enabling the quantitative investigation of such wall friction drag reduction control methods. However, these methods do not account for the streamwise geometry changes due to insufficient consideration of time translation symmetry (energy conservation). Therefore, there has been little discussion on the flow separation, wall friction change and severe heat flux caused by the SBLI induced by flow turning, such as compression ramp flows.

Due to the difference in initial flow states, maneuvering of the aircraft may result in multistable states of the flow, which is ubiquitous in aerospace flow systems [29]. Bistable states of SSIs between regular and Mach reflections are observed when varying the incident shock angle [30–34]. The underlying mechanism for this bistable behavior has been elucidated by Hu et al. through minimal viscous dissipation theory [35]. Recently, Hu et al. numerically observed bistable states of SBLI between separation and attachment in curved compression ramp (CCR) flows by varying the attack angle [29] and mathematically demonstrated their existence [36]. Multistable states can lead to quite different aerothermodynamic performance results, such as the lift and drag coefficients, wall parameters and the start margin of the inlet [37–42]. The mechanism of separation hysteresis and the aerothermodynamics associated with bistable states in CCR flows were thoroughly examined by Zhou et al. [43] and Tang et al. [44]. However, the origin of the disparities in the aerothermodynamic characteristics across multistable states needs further investigation.

The aim of this paper is to address the fact that the existing decomposition methods are limited in their applicability to complex geometries by proposing a decomposition method that satisfies local time translation symmetry and spatial translation symmetry. Moreover, this method can offer a unified framework for analyzing the generation mechanism of wall friction and heat flux for further guidance in researching their simultaneous control. Before deriving the decomposition method, the details of the numerical simulations are described in Section 2. Based on the local time translation symmetry and spatial rotation symmetry, a physically clear form of the wall friction and heat flux decomposition method, which can apply to a surface with a streamwise arbitrary curvature, as well as the verification of the method, is proposed in Section 3. The flow fields, the aerothermodynamic characteristics of

bistable states in CCR flows, and the mechanism of wall friction and heat flux generation are analyzed in Sections 4–6. The conclusions are drawn in Section 7.

2. Numerical Simulation

2.1. Governing Equations and Numerical Methods

Direct numerical simulations (DNSs) of laminar flows were carried out for the present analysis and implemented by the in-house code OPENCFD-SC, which has been successfully validated and applied to many cases [29,45–47]. The governing equations, formulated in a non-dimensionalized conservative form and expressed within the framework of curvilinear coordinates, are as follows:

$$\frac{\partial U}{\partial t} + \frac{\partial F}{\partial \xi} + \frac{\partial G}{\partial \eta} = 0 \tag{1}$$

with $U = J\{\rho, \rho u, \rho v, \rho e\}$ as the conservative vector flux, ρ as the density, (u, v) as the streamwise and vertical components of velocity, and $e = c_v T$ as the internal energy per volume. J is the Jacobian matrix transforming Cartesian coordinates (x, y) into a computational space defined by curvilinear coordinates (ξ, η). The flux term F in the ξ direction is composed of the convective term F_c and the viscous term F_v:

$$F = F_c + F_v = Jr_\xi \begin{bmatrix} \rho u^* \\ \rho u u^* + p s_x \\ \rho v u^* + p s_y \\ (\rho e + p) u^* \end{bmatrix} - Jr_\xi \begin{bmatrix} 0 \\ s_x \sigma_{xx} + s_y \sigma_{xy} \\ s_x \sigma_{yx} + s_y \sigma_{yy} \\ s_x \tau_x + s_y \tau_y \end{bmatrix} \tag{2}$$

where

$$\begin{aligned} &u^* = u s_x + v s_y, \quad s_x = \xi_x / r_\xi, \quad \tau_x = u\sigma_{xx} + v \\ &r_\xi = \sqrt{\xi_x^2 + \xi_y^2}, \quad s_y = \xi_y / r_\xi, \quad \tau_y = u\sigma_{xy} + v\sigma_{yy} - q_y, \\ &\sigma_{ij} = 2\mu \left[\frac{1}{2} \left(\frac{\partial u_i}{\partial x_j} + \frac{\partial u_j}{\partial x_i} \right) - \frac{1}{3} \frac{\partial u_k}{\partial x_k} \delta_{ij} \right], \\ &q_j = -\frac{\mu}{Pr(\gamma - 1) Ma_\infty^2} \frac{\partial T}{\partial x_j}. \end{aligned} \tag{3}$$

where $i, j = x, y$. G is the flux term in the η direction having similar forms to F [48]. The working fluid is an ideal gas, fulfilling the pressure condition $p = \rho T / \gamma Ma_\infty^2$, where $\gamma = 1.4$ is the ratio of specific heats, T the static temperature, and Ma the Mach number. The free-stream condition is denoted by the subscript "∞". The free-stream quantities are used to normalize the flow parameters ρ, u, p and T. The unit Reynolds number Re_∞ (m^{-1}) = 3×10^6 and Prandtl number $Pr = 0.7$. The viscosity μ fulfills Sutherland's law, $\mu = \frac{1}{Re_\infty} \frac{T^{3/2}(1+110.4/T_\infty)}{T+110.4/T_\infty}$, with $T_\infty = 108.1$ K as the free-stream static temperature.

2.2. Computational Domain and Flow Conditions

Curved compression ramps (CCRs), as shown in Figure 1, were selected for numerical simulation. The streamwise region x ranges from -82 mm to 108.9 mm ($x = -80$ mm is the start of the flat plate, and the extension line of the flat plate intersects the extension line of the tilted plate at $x = 0$ mm). The normalwise region y ranges from 0 mm to 40 mm. The flat plate and the tilted plate are linked by an arc wall with the curvature radius $R = \frac{L}{\sin \frac{\phi}{2}}$, where $L = 25$ mm, with the curved wall starting at $x = -L$ and with ϕ as the turning angle.

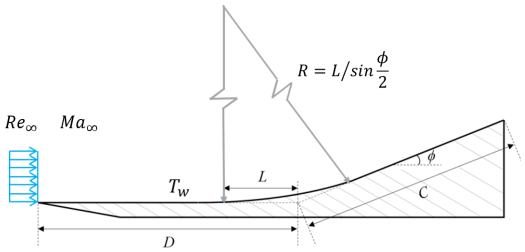


Figure 1. Sketch of curved compression ramp.

The algebraically generated computational mesh consists of 3401 × 401 nodes in the streamwise and normalwise directions, respectively. The streamwise grids consist of a uniformly spaced region with $\Delta x = 0.05$ mm and a buffer region containing 160 nodes with a stretch factor of 1.015. The normalwise grids are clustered in the near-wall region, with the first grid height $\Delta y = 0.01$ mm. The laminar boundary layer thickness $\delta|_{x=-50\text{mm}} \approx 0.5$ mm results in 41 points inside the boundary layer, ensuring good resolution.

The wall boundary conditions are set as no-slip and isothermal, with the wall temperature ratio given by $T_w = \hat{T}_w / T_\infty$, where $\hat{T}_w$ is the wall temperature and the subscript "w" represents the wall condition. A uniform inlet flow condition is applied at $x = -82$ mm. A non-reflecting boundary condition is applied at the outlet. Bistable states of CCR flows are obtained by altering ϕ and T_w, and the two series of DNSs conducted are summarized in Table 1.

Table 1. Flow and geometric conditions for the present simulations. (For each case, the attachment state and separation state, denoted by "Att" and "Sep", respectively, may exist with the same boundary condition and ramp angle but with different initial conditions.)

Ma_∞	T_w	ϕ (°)
6.0	1.5	17 (Att), 18 (Att/Sep), 19 (Att/Sep), 20 (Att/Sep), 21 (Att/Sep), 22 (Att/Sep), 23 (Att/Sep), 24 (Sep)
6.0	1.25 (Att), 1.5 (Att/Sep), 1.75 (Att/Sep), 2.0 (Att/Sep), 2.25 (Sep)	18

2.3. Convergence Study and Validation

A flat-plate ramp with a turning angle $\phi = 24°$ was selected for mesh convergence examination. The flow condition is $Ma_\infty = 6.0$ and $T_w = 1.5$ (denoted by IBC1 in the following). Time convergence will be discussed in Section 4. Four grid scales were selected, including 1201 × 141 (grid A), 1701 × 201 (grid B), 2401 × 281 (grid C) and 3401 × 401 (grid D). Surface pressure coefficient C_p distributions are shown in Figure 2, where $C_p = \frac{(p_w - p_\infty)}{\frac{1}{2}\rho_\infty u_\infty^2}$ and p_w is the wall pressure. The pressure plateau p_{pla} and pressure peak p_{pk} collapse well with that predicted by the minimal viscous dissipation (MVD) theorem [46]. As shown in Figure 2b, the separation point (the black circle) moves upstream, and the pressure rises with a denser grid. And, both the distributions of C_p and locations of the separation points of grids C and D collapse well, indicating that the mesh size of grid D is deemed adequate for the present analysis.

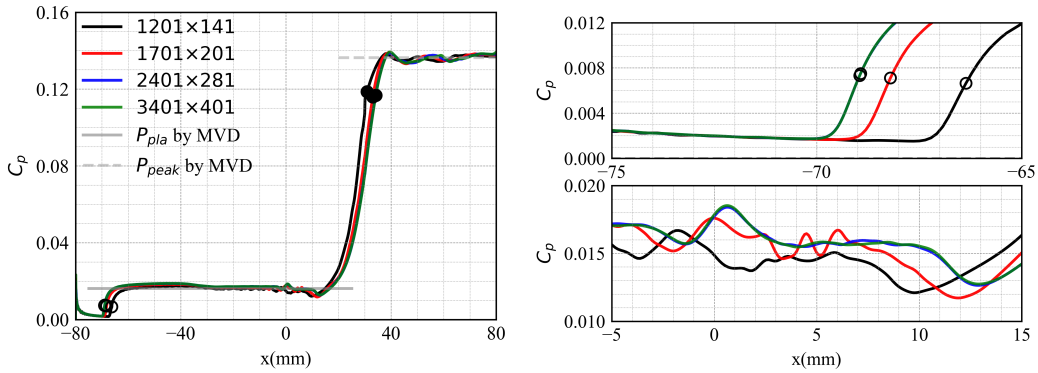


Figure 2. Four grid scales for mesh convergence examination by the case IBC1, $\phi = 24°$. (**a**) C_p distributions of four grid scales. The gray solid and dashed lines are the pressure plateau and pressure peak predicted by the MVD theorem [46], respectively. (**b**) Close-up plots of the separation and vertex regions.

The distributions of non-dimensionalized u and T in the normalwise direction inside the boundary layer are validated by comparison against theoretical Blasius solutions with compressible correction [49]. Good agreement validates the DNS results, as shown in Figure 3. Further validation with published experimental and numerical results can be found in Appendix A.

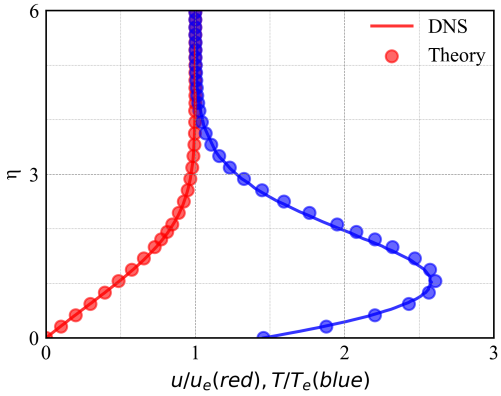


Figure 3. Comparison of u and T from DNS with theoretical predictions at $x = -43$ mm of the case IBC1, $\phi = 18°$, with the subscript "e" representing the external boundary layer flow.

3. Decomposition Method

Existing studies involving the simultaneous decompositions of wall friction and heat flux frequently employ a consistent decomposition methodology [25,50], and the most common one is the twofold repeated integration of the momentum and energy equations based on the the FIK identity [7]. By employing this method, individual physical mechanisms can be distinctly decoupled for analysis. However, the connection between wall friction and heat flux generation is not clear enough, as they are manifested through the distinct forms of momentum and energy, respectively. Therefore, it finds difficulty in guiding the efficient control of friction and heat flow simultaneously. Since all contributions in heat flux decomposition are in the form of energy, and the RD identity [9] is based on the work–energy conversion process between different mechanisms, the RD and FIK identities are adopted for wall friction and heat flux decompositions, respectively. In this way, the two decompositions are related from the perspective of energy. Noether's theorem [51–53] posits a profound relationship between conservation laws and the corresponding symmetries. Critical to the application of decomposition methods in fluid dynamics from the perspective

of energy is their adherence to the principle of time translation symmetry. This adherence ensures that the decomposition methods uphold energy conservation, thereby providing a robust physical basis for its application to flows across diverse surfaces. In addition, the clear energy conversion path [14,16] obtained by the method may help improve flow control efficiency. In the following, the decomposition methods of wall friction and heat flux for an arbitrary surface are introduced, and the unique and disambiguated selection of the integral order in the FIK identity and the Galileo transformation speed in the RD identity are clarified from the perspective of local time translation symmetry.

3.1. Derivation of Wall Friction Decomposition

Renard and Deck analyzed the work–energy conversion process in differential form in their paper (Equation (2.5) in Ref. [9]). On the basis of their idea, the present paper will further discuss this process from the perspective of energy conversion between the wall and flow and demonstrate the disambiguation of Galileo transformation velocity u_b, since the arbitrariness of u_b may lead to non-compliance with local energy conservation, which will be explained in detail in the following. The following derivation is based on the rotated equations of the coordinate system, which will be discussed in Section 3.3. Specifically, the Reynolds-averaged streamwise momentum equation is expressed as

$$\frac{\partial \overline{\rho u}}{\partial t} + \frac{\partial \overline{\rho u u}_j}{\partial x_j} = \frac{\partial \overline{\tau_{x,j}}}{\partial x_j} - \frac{\partial \overline{p}}{\partial x} \tag{4}$$

where "$^-$", ρ, u_j, $\tau_{x,j}$ and p represent the Reynolds average operator, density, velocity component, shear stress and pressure, respectively. This equation represents streamwise momentum conservation and satisfies spatial translation symmetry. So, we can follow the process of the RD identity [9,10] and adopt Galileo transformation with a speed of $-u_b$ to transform the reference frame from a stationary wall (the initial reference frame) to a moving wall (absolute reference frame). Then, the parameters in the absolute reference frame satisfy

$$t_a = t, \rho_a = \rho, x_a = x - u_b t, y_a = y, u_a = u - u_b, v_a = v \tag{5}$$

where the subscript "a" represents the variables in the absolute frame. The streamwise momentum equation in this reference frame can be obtained by substituting Equation (5) into (4):

$$\frac{\partial \overline{\rho u_a}}{\partial t_a} + \frac{\partial \overline{\rho_a u_a u_{aj}}}{\partial x_{aj}} = \frac{\partial \overline{\tau_{x,j}}}{\partial x_{aj}} - \frac{\partial \overline{p_a}}{\partial x_a} \tag{6}$$

Then, the energy budget equation of the averaged streamwise kinetic energy $K_a = 1/2\overline{\rho_a u_a u_a}$ in the absolute reference frame can be obtained by multiplying both sides of Equation (6) by $\tilde{u}_a$ and is expressed as

$$\frac{\partial \overline{K_a}}{\partial t_a} + \frac{\partial \overline{K_a u_{aj}}}{\partial x_{aj}} = \tilde{u}_a \frac{\partial \overline{\tau_{x,j}}}{\partial x_{aj}} - \tilde{u}_a \frac{\partial \overline{p_a}}{\partial x_a} \tag{7}$$

where the superscript "~" represents the Favre average operator. Integrating Equation (7) by parts over y from 0 to infinity and adopting the steady-state condition and non-slip condition on the wall, we can obtain the intermediate result as

$$u_b \bar{\tau}_w = \int_0^\delta \overline{\tau_{xy}} \frac{\partial \tilde{u}}{\partial y} dy + \int_0^\delta \frac{\partial \overline{K_a u_{aj}}}{\partial x_j} dy + \int_0^\delta \tilde{u}_a (-\frac{\partial \overline{\tau_{xx}}}{\partial x_a}) dy + \int_0^\delta \tilde{u}_a \frac{\partial \overline{p_a}}{\partial x_a} dy \tag{8}$$

and

$$u_b\bar{\tau}_w = \int_0^\delta \overline{\tau_{xy}}\frac{\partial\tilde{u}}{\partial y}dy + \int_0^\delta(\tilde{u}-u_b)[\frac{\partial\overline{\rho uu}}{\partial x}+\frac{\partial\overline{\rho uv}}{\partial y}]dy + \int_0^\delta(\tilde{u}-u_b)(-\frac{\partial\overline{\tau_{xx}}}{\partial x})dy + \int_0^\delta(\tilde{u}-u_b)\frac{\partial\overline{p}}{\partial x}dy \quad (9)$$

In the absolute reference frame with the moving wall and still flow after Galileo transformation, the boundary layer is generated by the moving wall because of the viscosity and non-slip condition. The left-hand sides of Equations (8) and (9) represent the work input from the wall to the fluid to maintain the boundary layer, and the work input should be equal to the work required for the wall of a vehicle to overcome frictional drag to ensure local energy conservation at any point T on the wall of a vehicle, as shown in Figure 4. The work by wall frictional drag at any point T in Figure 4 is equal to the product of the wall shear stress and velocity component in the direction of the force:

$$\mathrm{SW} = \vec{\tau}\cdot\vec{u}_\infty = \bar{\tau}_w u_\infty\cos\varphi \quad (10)$$

where SW is the wall shear stress work by wall friction, $\tau_w = \mu_w\frac{\partial u}{\partial y_n}|_{y_n=0}$ the wall shear stress, and φ the angle between the tangential direction of the local wall surface and $\vec{u}_\infty$. As discussed above, the left-hand side of Equation (9) should be equal to SW at point T to ensure local energy conservation. It should be emphasized that the above derivation and analysis focus on point T locally. And, the Galileo transformation is also implemented locally along the wall surface, which is different from the global transformation in the traditional RD identity [9,10]. The benefit of this approach is that local time translation symmetry is guaranteed. Therefore, this method has a clear physical interpretation in evaluating frictional drag reduction research for vehicles with complex configurations. According to the analysis of Equation (9), the Galileo transformation velocity u_b is unique and disambiguated as

$$u_b = u_\infty\cos\varphi \quad (11)$$

rather than arbitrary.

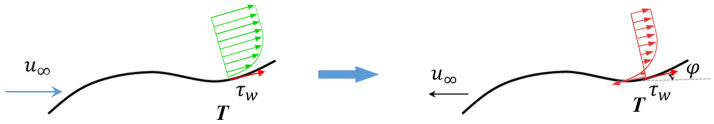


Figure 4. Schematic diagram of Galileo transformation on curved wall with boundary layer profile on it.

Combining Equations (9) and (11), as well as the definition of wall friction as $C_f = \frac{\overline{\tau_w}}{1/2\rho_\infty u_\infty^2}$, the final form of wall friction decomposition can be obtained as

$$C_f = \underbrace{\frac{2}{\rho_\infty u_\infty^3\cos\varphi}\int_0^\delta \overline{\tau_{xy}}\frac{\partial\tilde{u}}{\partial y}dy}_{C_f^L} + \underbrace{\frac{2}{\rho_\infty u_\infty^3\cos\varphi}\int_0^\delta(\tilde{u}-u_\infty\cos\varphi)[\frac{\partial\overline{\rho uu}}{\partial x}+\frac{\partial\overline{\rho uv}}{\partial y}]dy}_{C_f^{MT}} + \underbrace{\frac{2}{\rho_\infty u_\infty^3\cos\varphi}\int_0^\delta(\tilde{u}-u_\infty\cos\varphi)(-\frac{\partial\overline{\tau_{xx}}}{\partial x})dy}_{C_f^S} + \underbrace{\frac{2}{\rho_\infty u_\infty^3\cos\varphi}\int_0^\delta(\tilde{u}-u_\infty\cos\varphi)\frac{\partial\overline{p}}{\partial x}dy}_{C_f^P} \quad (12)$$

where the contribution terms for wall friction generation are the viscous dissipation C_f^L, the kinetic energy transport C_f^{MT}, the streamwise distortion C_f^S and the work performed

by the pressure gradient C_f^P. In the above derivations, φ is a local quantity to reflect the local wall shape. In addition, as previously mentioned, $\cos\varphi$ is a typical parameter to reflect the real local work performed by wall shear stress on a curved wall, which is quite different from the case of flat-plate flows. After non-dimensionalization, C_f represents the local wall shear work, which is converted into C_f^L, C_f^{MT} and C_f^S, while C_f^P can usually serve as a source (or sink) term, since C_f^P originates from the pressure gradient, which is generally induced by compression or expansion walls, or incident shocks. For an aircraft, C_f and C_f^P correspond to friction and wave resistance, respectively, and the conversion between C_f and C_f^P is achieved indirectly by C_f^L, C_f^{MT} and C_f^S. After decomposition, the generation mechanism of wall friction is decoupled into these quantified terms, which is crucial for understanding the relative importance of each effect and for designing targeted flow control strategies. Moreover, decomposition by the RD identity inherently satisfies energy conservation, providing a robust basis for analyzing the work–energy conversion process. Similar to Refs. [14,16], the whole energy conversion process can be depicted in Figure 5. With respect to this physical description, the wall friction decomposition method for arbitrary profiles is obtained.

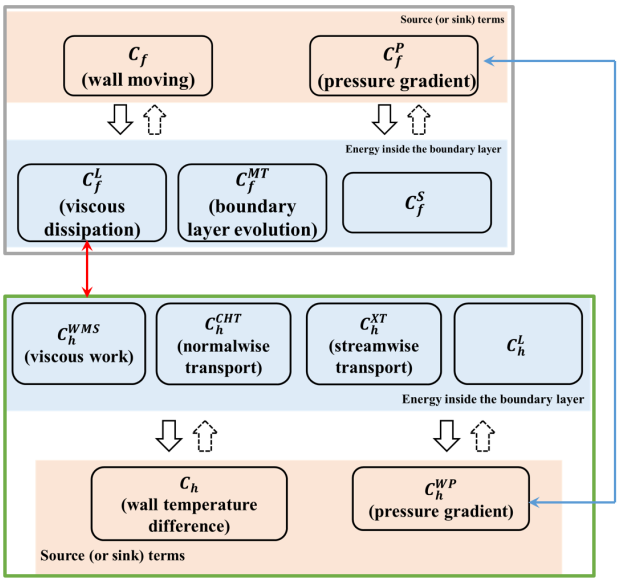


Figure 5. A schematic to illustrate the energy conversion pathways in the flow. The pathways in the gray and green boxes are based on the wall friction and heat flux decomposition methods, respectively. The red and blue arrows represent the links between the terms.

3.2. Derivation of Heat Flux Decomposition

For heat flux decomposition, we agree with the viewpoint of Zhang and Xia [21,22] and Wenzel et al. [25] that the twofold integration of the FIK identity has better interpretability. The following derivation is consistent with that of Zhang and Xia [21,22], but we will propose an explicit physical depiction and physical interpretation from the perspective of the redistribution of temperature (enthalpy) in the boundary layer. The equation for averaged static enthalpy is

$$\frac{\partial \overline{\rho e}}{\partial t} + \frac{\partial \overline{\rho h u_j}}{\partial x_j} = \frac{\partial \overline{q_j}}{\partial x_j} + \overline{\tau_{i,j}\frac{\partial u_i}{\partial x_j}} + \overline{u_j \frac{\partial p}{\partial x_j}} \tag{13}$$

where the static enthalpy $h = e + p/\rho = c_p T$, and the heat flux $\overline{q_j} = \overline{\kappa \partial T/\partial x_j}$.

For steady flows, integrating Equation (13) from the wall ($y|_w = 0$) to a distance y in the wall-normal direction and applying the no-slip condition $u_w = v_w = 0$ on the wall yields

$$q_w = q_y - \overline{\rho hv}\Big|_y + \int_0^y \overline{\tau_{i,j}\frac{\partial u_i}{\partial x_j}}dy_1 + \int_0^y u_j\frac{\partial p}{\partial x_j}dy_1 + \int_0^y -\frac{\partial \overline{\rho hu}}{\partial x}dy_1 \tag{14}$$

where q_w is the wall heat flux, and the terms on the right-hand side of Equation (14) are energy conduction at y, enthalpy transfer along the normal direction (convective heat transport, red arrow in Figure 6), the work by viscous stress, the work by the pressure gradient and enthalpy transport along the streamwise direction, respectively. This equation expresses the local equilibrium relation on the wall but also gives the essence of heat flux generation on the wall, namely, the redistribution of temperature (enthalpy) in the boundary layer along the normal direction. This process includes the local generation of enthalpy in the boundary layer and the transport along the streamwise and normal directions. In this case, the convective heat transport term $\overline{\rho hv}\Big|_y$ is the most obvious way to enhance the redistribution of the boundary-layer temperature along the normal direction, except q_y. And, the total normally convected enthalpy from the outer boundary layer to the wall (or in reverse) can be obtained by integrating this term from 0 to δ, with δ as the boundary layer thickness.

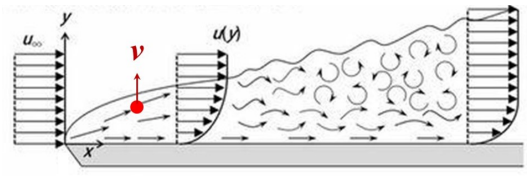


Figure 6. Normalwise enthalpy transfer.

Similar to the FIK identity and Zhang and Xia's derivation, by integrating Equation (14) by parts from 0 to δ along the wall-normal direction, we can obtain the final form of heat flux decomposition.

$$\begin{aligned} C_h = &\underbrace{\frac{1}{\rho_\infty u_\infty (h_{aw}-h_w)\delta}\int_0^\delta q_y dy}_{C_h^L} + \underbrace{\frac{1}{\rho_\infty u_\infty (h_{aw}-h_w)\delta}\int_0^\delta -\overline{\rho hv}dy}_{C_h^{\mathrm{CHT}}} \\ &+ \underbrace{\frac{1}{\rho_\infty u_\infty (h_{aw}-h_w)\delta}\int_0^\delta (\delta-y)\overline{\tau_{i,j}\frac{\partial u_i}{\partial x_j}}dy}_{C_h^{\mathrm{WMS}}} + \underbrace{\frac{1}{\rho_\infty u_\infty (h_{aw}-h_w)\delta}\int_0^\delta (\delta-y)u_j\frac{\partial p}{\partial x_j}dy}_{C_h^{WP}} \\ &+ \underbrace{\frac{1}{\rho_\infty u_\infty (h_{aw}-h_w)\delta}\int_0^\delta (\delta-y)\left(-\frac{\partial \overline{\rho hu}}{\partial x}\right)dy}_{C_h^{XT}} \end{aligned} \tag{15}$$

where the Stanton number $C_h = \frac{q_w}{\rho_\infty u_\infty (h_\infty + r u_\infty^2/2 - h_w)}$, and $r = \sqrt{Pr}$. This relation decouples the generation mechanism of the heat flux at the wall into five physical processes, including the heat transfer C_h^L, representing the energy transfer process achieved through molecular motion due to the temperature gradient; the convective heat transport C_h^{CHT}, representing the transport of enthalpy along the normal direction brought by the flow; the work from viscous stress C_h^{WMS}, representing the energy corresponding to the deformation of fluid microclusters and viscous dissipation caused by viscous stresses, where viscous dissipation leads to the loss of flow kinetic energy, which is converted into internal energy, resulting in an increase in local temperature; the pressure gradient C_h^{WP}, representing the energy corresponding to the deformation of fluid microclusters and viscous work by pressure gradients induced by shock waves; and streamwise enthalpy transport C_h^{XT}, representing

the net increase in local enthalpy caused by the flow along the streamwise direction. Focusing on a certain location within the boundary layer, a significant portion of C_h^{WMS} is dissipated and converted into internal energy, leading to an increase in local temperature. According to the Reynolds analogy for an undisturbed boundary layer [54], changes in temperature within the boundary layer are closely related to changes in velocity, which, in turn, can cause variations in the local streamwise and normalwise velocities. The increased temperature will be transported by the altered velocities in both the streamwise and normalwise directions by C_h^{XT} and C_h^{CHT}. Specifically, C_h^{CHT} will further lead to a redistribution of the temperature profile within the boundary layer. This redistribution results in changes in the near-wall temperature gradient, thereby altering the local wall heat flux. In the strongly perturbed flows caused by SBLI, this process still holds. The work by APG injects much higher energy, and its impact on this process is more significant. The decomposition method used in this paper can obtain a comprehensive effect of this process through integration.

Comparing Equations (12) and (15), we can find that the integrated terms in $C_f^L \backslash C_h^{WMS}$ and $C_f^P \backslash C_h^{WP}$ are quite similar and represent the same energy generation mechanism. Therefore, the combined decomposition method links the generation of C_f and C_h from the perspective of energy conversion, as shown in Figure 5. And, one benefit of the method is that it provides a helpful evaluation tool for the simultaneous flow control of wall friction and heat flux.

3.3. Mesh-Independent Data Transformation Method for Arbitrary-Curvature Surface

According to the definition, the integrated terms in the wall friction and heat flux decompositions should be integrated along the wall-normal direction to ensure local time translation symmetry. The existing wall friction and heat flux decomposition analyses are usually established on quasi-two-dimensional profiles, such as flows on flat plates and in channels, and the integration along the wall-normal direction can be directly carried out along the grid lines, while the transformation of the flow field is needed for arbitrary-curvature profiles, since the vertical grid lines are not perpendicular to the wall. The transformation methods include using coordinate scaling, applying coordinate rotation, or directly dealing with the equations in curved surface coordinates.

- Coordinate scaling can be carried out by Jacobi transformation, i.e., transforming the flow field of any shape into a square, and then integration along grid lines with the Jacobian matrix is feasible, as the grid lines have been transformed to the wall-normal component.
- If we directly deal with the equations in the curved coordinate system, the equations are clear (Equation (16)). However, it is somewhat difficult to sort out the format of the grids for integrating these equations.

$$\rho\left[\frac{u_s}{h}\frac{\partial u_s}{\partial s}+u_n\frac{\partial u_s}{\partial n}+\frac{\kappa u_s u_n}{h}\right]=-\frac{1}{h}\frac{dp}{dx}+\frac{\partial \tau}{\partial n} \tag{16}$$

- The rotation of the computational domain with the given angle of the local slope satisfies spatial rotational symmetry and is also a feasible method. That is, the flow field is rotated to the concerned direction without changing the essence of the inertial system (Figure 7). This method is selected for the present analysis.

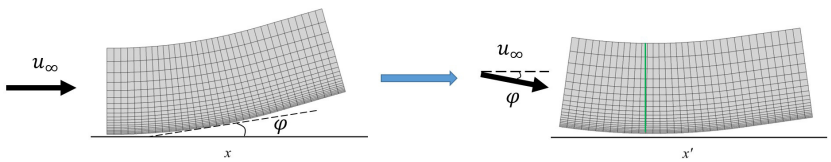
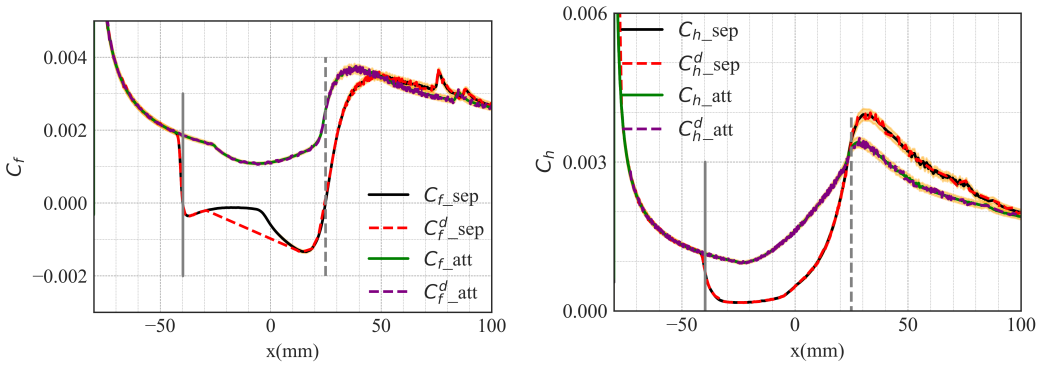


Figure 7. Coordinate rotating diagram.

The selection of the integral path direction is discussed below. Except for the definition, although the information on grid lines can transform to the normal position of the wall, it represents the upstream or downstream information of the actual position. In addition, the integral results will be associated with a grid set and may not be unique. Therefore, integration along the wall-normal direction may be a better choice to obtain the real wall friction and heat flux decomposition results. Specifically, grid interpolation can be performed; that is, a local normal grid is set (green line in Figure 7), along which the flow field is interpolated to obtain flow parameters along the normal direction.

3.4. Decomposition Method Verification

The wall friction C_f and heat flux C_h are determined through their definitions or Equations (12) and (15), which reflect the wall quantity and the overall effects inside the boundary layer, respectively. Figure 8 compares the results obtained by their definitions and Equations (12) and (15) (tagged with the superscript "d") with the conditions of IBC1, $\phi = 18°$, between the DNSs and decompositions. The relative errors (calculated by $error = |(C_m^d - C_m)/C_m| \times 100\%$ with $m = f, h$ representing the wall friction and heat flux, respectively) are within 3%. The small error indicates that the decomposition method offers a correct estimation of the overall effects inside the boundary layer on C_f and C_h. Further comparisons of the contribution terms with theoretical solutions are carried out and discussed in Sections 5 and 6.



(**a**) (**b**)

Figure 8. A comparison of the results with the conditions of IBC1, $\phi = 18°$, between the numerical simulations and the decomposition (tagged with the superscript "d") of (**a**) wall friction and (**b**) heat flux (the orange area is the 3% error band, and the separation and attachment states are denoted by the subscripts "sep" and "att", respectively.) The vertical solid and dashed gray lines represent the streamwise locations of separation and reattachment points, respectively.

4. Bistable States of CCR Flows

The bistable states characterized by flow separation and attachment are achieved through variations in ϕ and T_w, as shown in Figure 9. For the ϕ-variation-induced bistable states, only the steady attachment flow state exists when $\phi = 17°$, as shown in Figure 9b. Increasing ϕ with $\Delta\phi = 1°$ after the flow reaches convergence and using it as the initial condition (state Att_$\phi = 17°$ to Att_$\phi = 23°$ in Figure 9a), the attachment state is maintained until $\phi = 23°$. However, a sudden flow separation occurs when $\phi = 24°$. In the opposite process of decreasing ϕ from 24° with the same $\Delta\phi$, the flow remains separated until $\phi = 17°$, at which point the attachment state suddenly appears again. The interval ($\phi_{att} = 17°$, $\phi_{sep} = 24°$) is the bistable state interval (BSI, as shown in the green square in Figure 9a) for the current inlet and boundary conditions (IBCs), in which the same IBCs may result in either separation or attachment flow states, contingent upon varying initial conditions.

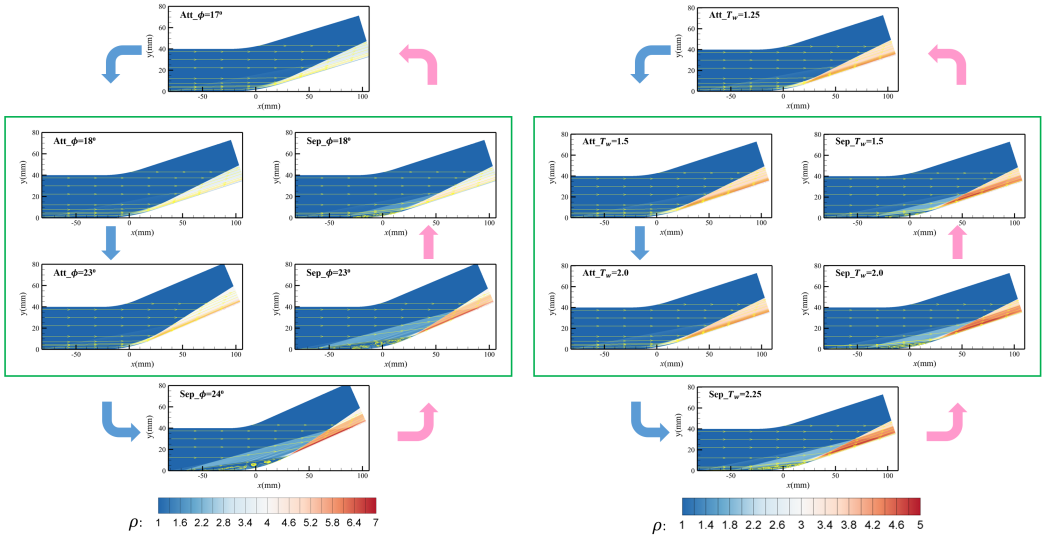


Figure 9. Bistable states of separation/attachment achieved through (**a**) ϕ variation with the condition IBC1 and (**b**) T_w variation with the conditions $Ma_\infty = 6.0$, $\phi = 18^\circ$, colored by the local density. The streamlines are represented by golden lines with arrows. Inside the green square is the bistable state interval.

Bistable states induced by T_w variation are obtained in a similar process, as shown in Figure 9b. Starting with the attachment flow state of $T_w = 1.25$, the attachment state is maintained up to a threshold value of $T_w = 2.0$ when increasing T_w by $\Delta T_w = 0.25$. Beyond this threshold, specifically at $T_w = 2.25$, the flow state transitions to a distinct separation state. Decreasing T_w from $T_w = 2.25$ by the same ΔT_w, the separation state is maintained until $T_w = 1.5$. And, only the attachment state exists with $T_w = 1.25$. Therefore, the BSI is ($T_{w,att} = 1.25$, $T_{w,sep} = 2.25$) in this case.

The differences in C_f and C_h between bistable states are distinct, as shown in Figure 8. The separation state has a negative C_f and a higher peak C_h, and the reasons for these differences will be discussed in the following. More discussions about the differences in aerothermodynamic characteristics between bistable states can be found in Refs. [43,44].

The separation length L_{sep} is continuously observed to ascertain time convergence, where

$$L_{sep} = x_{reatt} - x_{sep} \tag{17}$$

with x_{reatt} and x_{sep} as the streamwise locations of reattachment and separation points, respectively. Figure 10 illustrates the evolution of separation lengths as the flow transitions from separation to attachment ($\phi 18^\circ$ _sep _ to _ $\phi 17^\circ$, with "$\phi 18^\circ$ _sep" representing the separation state of CCR at $\phi = 18^\circ$) and from attachment to separation ($\phi 23^\circ$ _att _ to _ $\phi 24^\circ$). Starting from the attachment state, the flow separates after about 1000 τ (dimensionless time $1\tau = 1/(Ma_\infty \sqrt{\gamma R_g \hat{T}_{ref}})$), or equivalently, about five flow-through times on the ramp, but takes a long time to converge. The separation flow state is considered steady when the change in L_{sep} is below 0.01 mm over a time interval of 1000 τ. Starting from the separation state, L_{sep} drops to zero quickly after about 8000 τ and finally converges to zero. Therefore, the time convergence and the steady state are verified. For other cases, enough flow-through time is also carried out to ensure time convergence.

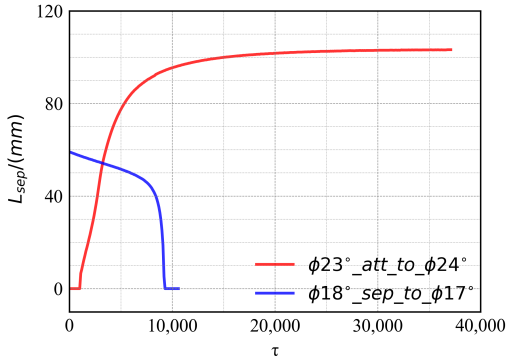


Figure 10. Time convergence process of separation length L_{sep} for IBC1. The suffixes "_sep" and "_att" denote flow states of separation and attachment, respectively.

5. Streamwise Evolution of C_f

The decomposition method and the data have been verified in the previous sections. In this section, the streamwise evolution of the contribution terms for C_f in Equation (12) at different locations (including the equilibrium flow region upstream of the origin interaction point, the separation region around the separation point, and the reattachment and peak wall friction region around the reattachment and peak wall friction points) are analyzed, as shown in Figure 11. It should be emphasized that for the wall friction decomposition, the following analysis takes place in the absolute reference frame by the Galilean transformation. That is, the boundary layer is generated by the moving wall, and the work from wall motion is a major source of the energy contained in the boundary layer, as described in Equations (10) and (12).

In the equilibrium flow region (Figure 11a), the flow remains undisturbed and attached. We further validate the decomposition results with theoretical Blasius solutions [49] (depicted by the scatters) in this region. The good agreement of each contribution term verifies the reliability of the decomposition analysis results. Moreover, we believe that the results of the separation and reattachment regions are reliable. From the distributions of the contribution terms, the dominant factor for wall friction generation is the viscous dissipation C_f^L, which indicates that the work performed by wall friction from the vehicle to the boundary layer is mainly dissipated by viscous stresses. The streamwise kinetic energy transport C_f^{MT} plays a secondary role, consistent with the streamwise progression of the boundary layer, as the boundary layer thickens and the kinetic energy contained in the boundary layer increases. But, the increase in kinetic energy also shows a gradual downward trend.

In the separation region (Figure 11b), the attachment state maintains the characteristics of the equilibrium flow region, since the flow is not disturbed. The wall friction of the separation state obviously decreases, which is the combined effect of C_f^{MT} and the work performed by the adverse pressure gradient (APG) C_f^P. Considering the energy conversion process shown in Figure 5, the positive and negative values of the contributions on the right-hand side of Equation (12) signify the direction of energy conversion, and a positive term indicates that the work by wall friction is converted into this contribution term, while a negative term is the opposite. Then, the negative C_f^P caused by the separation shock wave indicates that the work by the APG is injected into the boundary layer. Since the streamwise pressure gradient $\partial p/\partial x$ induced by shock waves is positive, and $\tilde{u} \leq u_\infty \cos\varphi$ inside the boundary layer, $C_f^P = \frac{2}{\rho_\infty u_\infty^3 \cos\varphi} \int_0^\delta (\tilde{u} - u_\infty \cos\varphi) \frac{\partial \overline{p}}{\partial x} dy$ around the separation and reattachment shock waves is always negative. Therefore, we refer to the absolute value of C_f^P when we talk about it in the following discussion. The APG will inevitably change the boundary-layer velocity profile, which is manifested as the obvious increase in kinetic energy in the boundary layer, as shown by the solid blue line in Figure 11b. The distortion of the velocity profile will also lead to local shear enhancement and result in higher C_f^L

(solid red line in Figure 11b). In this region, C_f^P and C_f^L are the two major contribution terms in the energy conversion process. The work performed by the APG leads to a significant decrease in the requirement for the work by the wall friction to maintain the boundary layer and even results in negative work by local wall friction, i.e., flow separation.

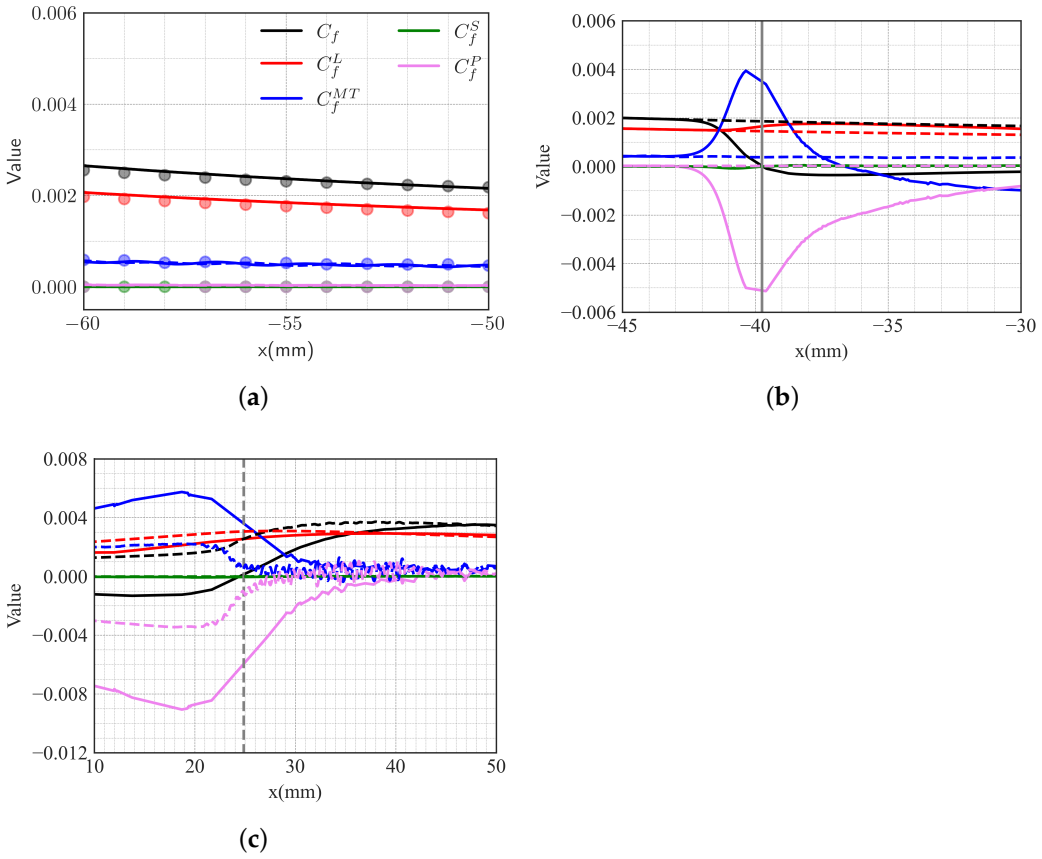


Figure 11. A comparison of different terms in the wall friction decomposition of separation/attachment states at different streamwise positions with the conditions of IBC1, $\phi = 18°$. The vertical solid and dashed gray lines indicate the streamwise separation and reattachment locations, respectively. The other solid and dashed lines indicate separation and attachment states, respectively. (**a**) The equilibrium flow region, with the scatters representing the results obtained theoretically; (**b**) the separation region; (**c**) the reattachment and peak wall friction region.

The relations of different contribution terms in the reattachment region (Figure 11c) are similar to those in the separation region, where C_f^P induced by the reattachment shock wave plays the dominant role. Specifically, the stronger intensity of the reattachment shock leads to a higher C_f^P.

As delineated in Equation (12), C_f^P is the coupling between the APG and the boundary-layer velocity profile, which will be affected by the wall temperature, thereby indirectly affecting C_f^P and the distribution of C_f. To elucidate the impact of the boundary-layer velocity profile on these parameters, it is advantageous to juxtapose the results from attachment states that share identical ramp angles and inlet Mach numbers but exhibit distinct wall temperature ratios T_w, as shown in Figure 12. In the equilibrium flow region ($x \leq -25$ mm), where the pressure gradient is nearly 0, the terms of wall friction decomposition are not affected by T_w variation, indicating that C_f^L, C_f^{MT} and C_f^S are independent of T_w. On the curved wall, with the increase in T_w, the minimum of C_f obviously decreases, and the reduction is primarily attributed to the escalation of C_f^P. Since the pressure rise on the surface is under nearly isentropic compression [43], the pressure gradient distribution is basically the same and independent of the wall temperature in these cases. The increase

in C_f^P with higher T_w reflects a larger velocity profile deficit, which is consistent with the higher shape factor discussed by Zhou et al. [43]. However, C_f^L is nearly unaffected by T_w variation. Therefore, it is more difficult to dissipate the energy injection by the APG for higher T_w, and the flow is more likely to separate.

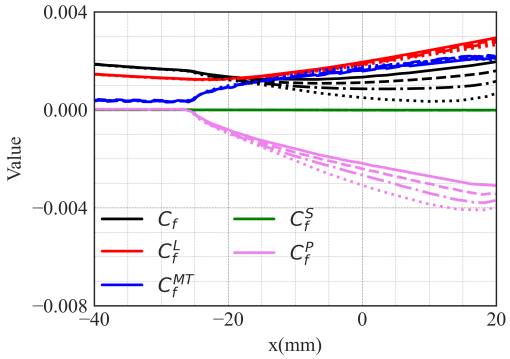


Figure 12. A comparison of the terms in the wall friction decomposition of attachment states with the conditions of $Ma_\infty = 6.0, \phi = 18°$, but different T_w (solid lines: $T_w = 1.25$; dashed lines: $T_w = 1.5$; dash-dot lines: $T_w = 1.75$; dotted lines: $T_w = 2.0$).

From Figures 11b,c and 12, C_f^{MT} and C_f^P are obviously highly correlated at the separation and reattachment regions of separation states or the curved walls of attachment states. The anti-correlation between them indicates that most of C_f^P is converted into C_f^{MT}, which is the conversion inside mechanical energy. Then, we add C_f^{MT} and C_f^P to obtain the mechanical energy transport term C_f^{ME}, i.e., $C_f^{ME} = C_f^{MT} + C_f^P$, to further investigate the energy conversion process, as shown in Figure 13. Similar to the previous discussion, the negative mechanical energy also means that the work performed by the APG supplies the mechanical energy input into the boundary layer.

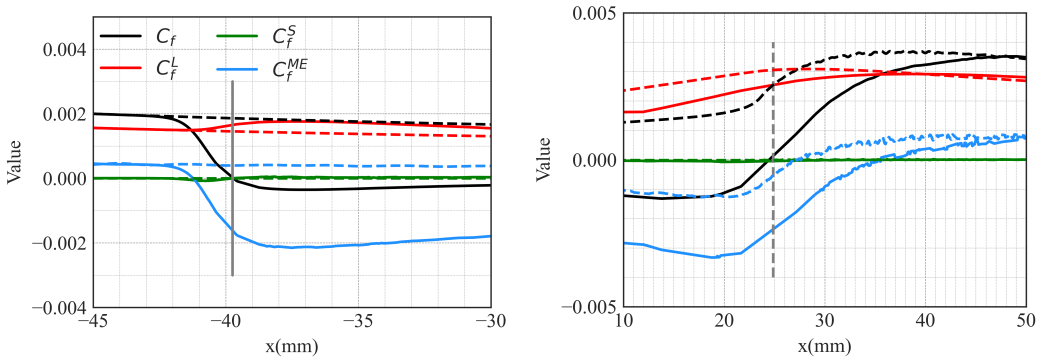


Figure 13. A comparison of the terms in wall friction decomposition in the mechanical energy form at different streamwise positions with the conditions of IBC1, $\phi = 18°$. The vertical solid and dashed gray lines indicate the streamwise separation and reattachment locations, respectively. The other solid and dashed lines indicate separation and attachment states, respectively. (**a**) The separation region; (**b**) the reattachment and peak wall friction region.

Figure 11b illustrates that the reduction in wall friction prior to the separation point is mainly caused by C_f^P. Figure 13 shows more clearly that the viscous dissipation increases slightly; therefore, it is difficult to dissipate further mechanical energy input, which results in a decrease in C_f (non-dimensionalized SW) until the flow separates. So, a key to keeping the boundary layer attached is the dissipation of the mechanical energy input via viscous dissipation. In the reattachment region, viscous dissipation obviously increases, and the

mechanical energy input starts to decrease after the reattachment shock wave, so an increase in wall friction is needed to maintain the boundary layer. The coupling of C_f^L and C_f^{ME} leads to the appearance of peak wall friction, and C_f^L is the principal contribution term in the generation of C_f after the reattachment point. The enhanced reattachment shock, triggered by an increased ramp angle ϕ, leads to reduced minimum wall friction within the separation bubble, as illustrated in Figure 14. This reduction is primarily attributed to the significant disparity in C_f^{ME}. However, it is noteworthy that the peak wall friction remains largely unaffected by variations in C_f^{ME}.

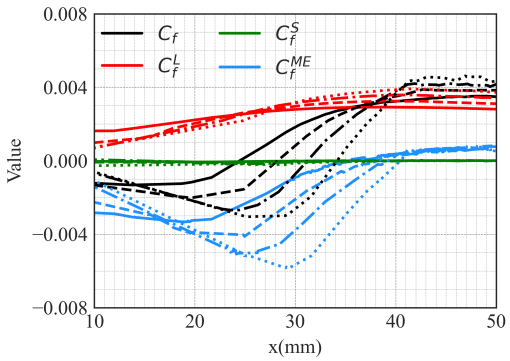


Figure 14. Effect of ramp angles on wall friction decomposition results of separation states at reattachment position (solid lines: $\phi = 18°$; dashed lines: $\phi = 20°$; dash-dot lines: $\phi = 22°$; dotted lines: $\phi = 24°$).

6. Streamwise Evolution of C_h

The analysis of wall heat flux decomposition takes place in the initial reference frame, different from the above analysis of C_f. The streamwise evolution of each contribution term is also analyzed first to elucidate the generation mechanism of heat flux C_h, as shown in Figure 15. For different regions, the heat transfer term C_h^L is very small and can be neglected, which represents a notable divergence from the results of Sun et al. [23]. They adopted the RD identity, resulting in the heat transfer weighted by the normal gradient of streamwise velocity, which will amplify the near-wall heat transfer. However, in the present analysis, C_h^L is the summation of heat transfer across the boundary layer. The difference may originate from these factors. In the equilibrium flow region (Figure 15a), we also validate the decomposition results with theoretical Blasius solutions [49] (depicted by the scatters). Good agreement of each contribution term is also obtained, verifying the reliability of the heat flux decomposition analysis results. From the distributions of the contribution terms, the convective heat transport term C_h^{CHT}, the viscous stress work term C_h^{WMS} and streamwise enthalpy transport term C_h^{XT} gradually decrease as the boundary layer develops. Although C_h^{CHT} convects the enthalpy outward from the wall to the outer flow, C_h^{XT} will supplement these parts. In addition, C_h^{WMS} is higher than C_h, so it can be inferred that the enthalpy convection along the normal direction by C_h^{CHT} is higher than the streamwise accumulation. In other words, C_h^{CHT} exerts a more pronounced influence on the generation of C_h.

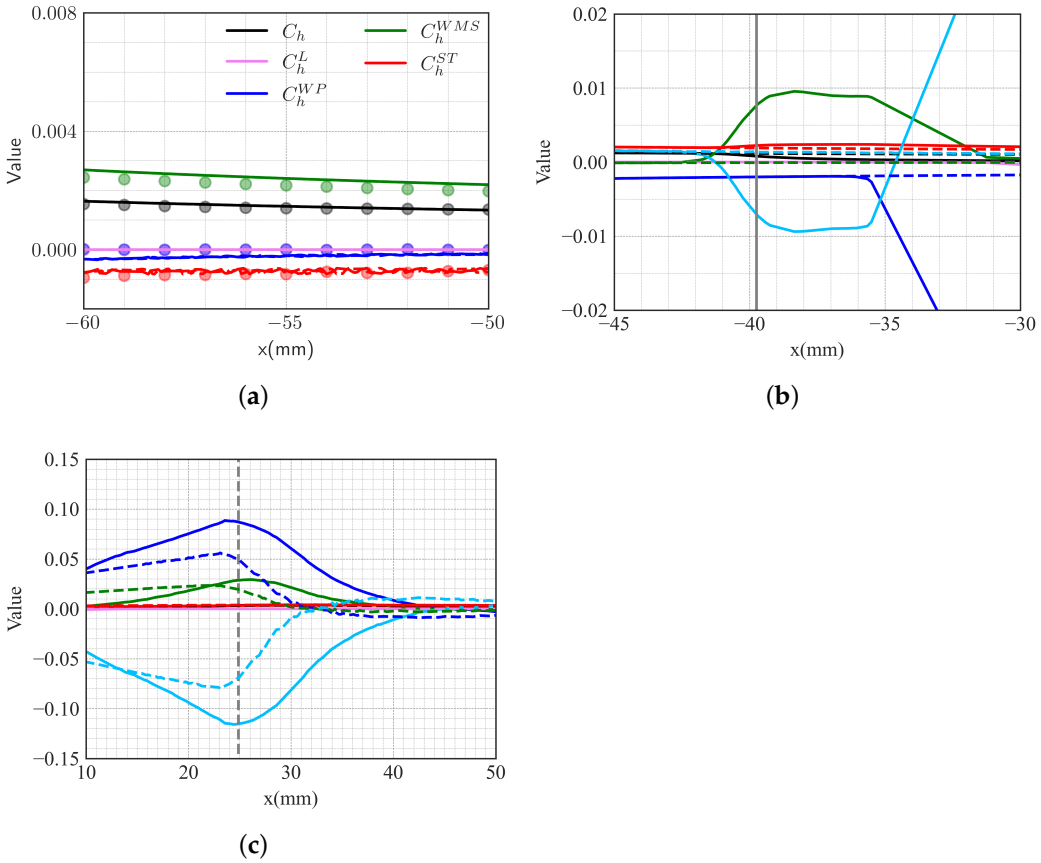


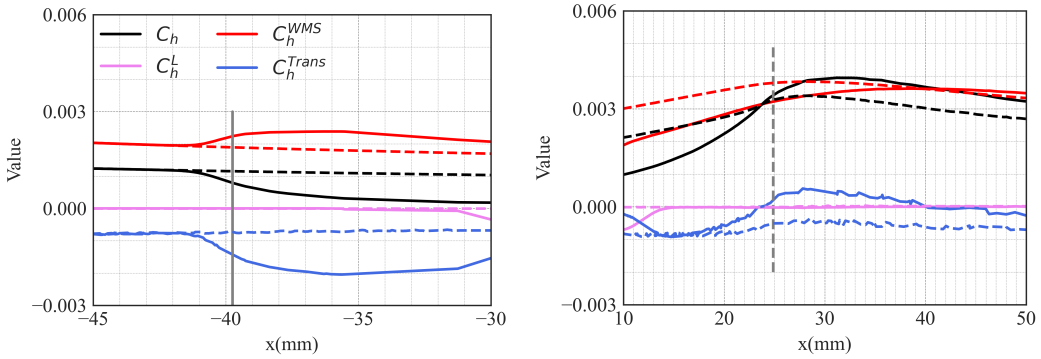
Figure 15. A comparison of different terms in the heat flux decomposition of separation/attachment states at different streamwise positions with the conditions of IBC1, $\phi = 18°$. The vertical solid and dashed gray lines indicate the streamwise separation and reattachment locations, respectively. The other solid and dashed lines indicate separation and attachment states, respectively. (**a**) The equilibrium flow region, with the scatters representing the results obtained theoretically; (**b**) the separation region; (**c**) the reattachment and peak heat flux region.

In the separation region (Figure 15b), similar to the previous analysis of C_f, prominent work by the APG C_h^{WP} originating from the separation shock wave can be found. Different from the results of wall friction decomposition, C_h^{WP} in heat flux decomposition presents as positive work and directly inputs energy into the boundary layer. Within the interval from the origin interaction point, located at approximately $x = -41$ mm, to the region where the boundary layer begins to noticeably deflect, situated at approximately $x = -36$ mm, the energy input associated with C_h^{WP} is transported downstream along the flow direction. This transport predominantly occurs through the streamwise enthalpy transport C_h^{XT}, which accounts for a larger proportion of the energy transfer. Consequently, this leads to a reduction in the wall heat flux. Furthermore, at $x > -36$ mm, an escalation in the normal velocity within the boundary layer contributes to a significant decrease in C_h^{CHT}. A very interesting phenomenon in this area is that C_h^{CHT} and C_h^{XT} together lead to an energy reduction, rather than anti-correlation between them in the equilibrium flow region. The energy input by C_h^{WP} accelerates the enthalpy transport, while the change in C_h^{WMS} is small, which is consistent with the results of the wall friction decomposition analysis.

In the reattachment and peak heat flux region (Figure 15c), C_h^{CHT} plays a positive role in the increase in wall heat flux as a consequence of the shear layer's impingement during the reattachment process of the separation state, and its value is significantly larger than those of C_h and C_h^{WP}. However, most of this energy is transported downstream by C_h^{XT}. For

the attachment state, C_h^{CHT} also directs energy to the wall as the flow deflection falls behind the wall shape, but the amount is significantly lower than that of the separation state.

Comparing the values and distributions of C_h^{CHT}, C_h^{XT} and C_h^{WP}, we can find that these terms always exhibit quasi-balance characteristics. In addition, the sum of C_h^{CHT} and C_h^{XT} is the local enthalpy variation. Here, we sum the three terms as the energy transport term C_h^{Trans}, i.e., $C_h^{Trans} = C_h^{CHT} + C_h^{XT} + C_h^{WP}$. And, the distributions are shown in Figure 16.



(a) **(b)**

Figure 16. A comparison of different terms in wall heat flux decomposition in the energy transport form at different streamwise positions with the conditions of IBC1, $\phi = 18°$. The vertical solid and dashed gray lines indicate the streamwise separation and reattachment locations, respectively. The other solid and dashed lines indicate separation and attachment states, respectively. (**a**) The separation region; (**b**) the reattachment and peak heat flux region.

In the separation region, although C_h^{WMS} increases to offer more enthalpy, C_h continues to decrease, which aligns with the results of Sun et al. [23]. The reason is that the additionally generated enthalpy is transported by C_h^{Trans}, as shown in Figure 16a. In the peak heat flux region (Figure 16b), C_h^{WMS} dominates the wall heat flux generation. This result indicates that, although the enthalpy brought by the impinging flow is large and the work induced by the APG is also considerable, most of them are transported downstream, and little is left locally. For the attachment state, C_h^{Trans} remains nearly constant along the streamwise direction. As a result, the streamwise positions of peak wall heat flux and peak C_h^{WMS} are nearly the same as those of the attachment state, while the position of the peak heat flux of the separation state is affected by C_h^{Trans}. In addition, the difference in the peak heat flux between the separation and attachment states is mainly attributed to C_h^{Trans}. A larger C_h^{Trans} results in higher peak heat flux in the separation state, although the C_h^{WMS} associated with the attachment state within the vicinity of the peak heat flux is a little higher than that of the separation state.

The influences of the ramp angle and wall temperature ratio on the contribution terms to wall heat flux generation are illustrated in Figure 17a and Figure 17b, respectively. With the increase in the ramp angle, C_h^{WMS} increases slightly. In contrast, the increase in C_h^{Trans} is more obvious, and the increase in peak heat flux is primarily caused by C_h^{Trans}. However, the difference in wall temperature has less influence on C_h^{WMS} and C_h^{Trans}. The results indicate that the increase in C_h^{WMS} is mainly caused by the enhanced distortion of the velocity profile induced by a stronger APG, while the influence of the changed molecular viscosity caused by different wall temperature ratios is small.

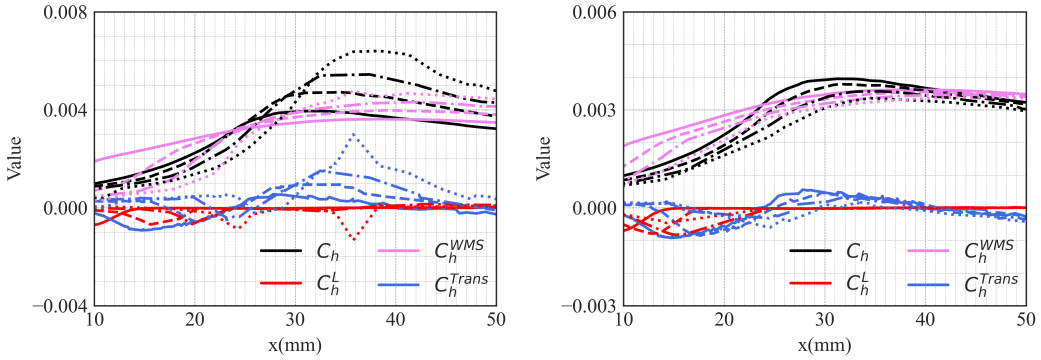


Figure 17. A comparison of decomposition in energy transport forms of separation states in peak heat flux region. (**a**) The influence of ramp angle (solid lines: $\phi = 18°$; dashed lines: $\phi = 20°$; dash-dot lines: $\phi = 22°$; dotted lines: $\phi = 24°$); (**b**) the influence of T_w (solid lines: $T_w = 1.5$; dashed lines: $T_w = 1.75$; dash-dot lines: $T_w = 2.0$; dotted lines: $T_w = 2.25$).

Compared with the results in Section 5, viscous dissipation/work dominates the generation of peak wall friction and peak heat flux. Therefore, one control method to simultaneously decrease peak wall friction and peak heat flux may be altering the matching of the velocity profile and stress distribution there to reduce the work by viscous stresses.

7. Conclusions

This study presents a significant advancement in the analysis of wall friction and heat flux in complex configurations, overcoming the resistance of existing decomposition methods that are suitable only for quasi-two-dimensional configurations. This decomposition method, which incorporates local time translation symmetry and spatial rotational symmetry, allows for a more accurate and comprehensive understanding of the generation mechanisms of wall friction and heat flux in complex flow configurations. This approach incorporates a specific Galilean transformation parameter that considers the variation in the wall slope. Based on the proposed decomposition method, the generation mechanism of the wall friction and heat flux of bistable states of curved compression ramp flows is investigated.

The generation of wall friction is dominated by viscous dissipation and the work by the adverse pressure gradient (APG). Moreover, these two contribution terms are correlated. The separation process is depicted from the perspective of energy conversion. In the absolute reference frame where the flow is still, the work by the APG will input energy into the boundary layer, a large proportion of which is converted into kinetic energy, while the remaining portion should be dissipated by viscous stresses; otherwise, the flow will be separated. The generation of peak wall friction is dominated by viscous dissipation.

The peak heat flux is primarily induced by the work of viscous stress. In the separation–reattachment process caused by shock-wave/boundary-layer interactions, although the energy brought by shear-layer impinging is high, most of the energy is transported downstream. However, the difference in peak heat flux between the separation and attachment states is mainly caused by energy transport. In addition, the impact of energy transport on the generation of peak heat flux increases with the increase in the ramp angle, i.e., a more intense APG, while viscous dissipation varies much less during this process.

The inherent symmetry within this analytical approach facilitates its straightforward extension to the evaluation of any three-dimensional engineering configuration, with a more accurate and reasonable interpretation of wall friction and heat flux generation. A key innovation of this work is the potential for the simultaneous control of wall friction and heat flux, originating from the unified framework that links these phenomena through energy conversion within the method, in contrast to existing methods, which often focus

on isolated aspects of the flow, such as skin friction or heat flux independently. Therefore, a further research endeavor involves conducting flow control studies aimed at reducing wall friction and heat flux simultaneously. Given that both peak wall friction and heat flux are primarily driven by viscous dissipation, diminishing this dissipative effect emerges as a promising strategy for achieving concurrent reductions in these parameters. However, it is crucial to recognize that a reduction in viscous dissipation could potentially compromise the boundary layer's capacity to resist the APG. Therefore, this method may serve as a valuable tool in exploring more efficient control methodologies that balance the reduction in wall friction and heat flux with the maintenance of adequate boundary-layer resilience against the APG.

Author Contributions: Conceptualization, M.T. and Y.H.; methodology, M.T., W.Z. and Y.H.; software, M.T. and Y.H.; validation, M.T., W.Z. and Y.H.; formal analysis, M.T. and W.Z.; investigation, M.T. and W.Z.; resources, G.W. and Y.Y.; data curation, M.T. and W.Z.; writing—original draft preparation, M.T.; writing—review and editing, Y.H., G.W. and Y.Y.; visualization, M.T., W.Z. and Y.H.; supervision, Y.H., G.W. and Y.Y.; project administration, G.W. and Y.Y.; funding acquisition, Y.Y. All authors have read and agreed to the published version of the manuscript.

Funding: This work was supported by the National Key R & D Program of China (Grant No. 2019YFA0405300) and the National Natural Science Foundation of China (Grant Nos. 12102449 and 12302309).

Data Availability Statement: The data that support the findings of this study are available from the corresponding author upon reasonable request.

Acknowledgments: We are grateful to Xi Chen of Beihang University and Dong Sun for their helpful discussion.

Conflicts of Interest: The authors declare no conflicts of interest.

Abbreviations

The following abbreviations are used in this manuscript:

SBLI	Shock-wave/boundary-layer interaction
CCR	Curved compression ramp
FIK	Fukagata, Iwamoto and Kasagi
RD	Renard and Deck
DNS	Direct numerical simulation
BSI	Bistable state interval
APG	Adverse pressure gradient

Appendix A. Further Validation of the Numerical Simulation

The selected compression ramp configuration with $\phi = 15^\circ$ is consistent with the Aachen shock tube TH2 experiment [55]. The flat plate and the inclined plate both exhibit a length dimension of $L = 100$ mm. The Reynolds number $Re_\infty(m^{-1}) = 4.2 \times 10^6$. Ma_∞ and Pr are 7.7 and 0.7, respectively. The wall boundary condition is no-slip and isothermal with a wall temperature ratio $T_w = 2.344$. Uniform inflow at a 0° attack angle is specified as the inlet condition. The computational mesh of the case is 1021×251.

The Mach number distributions in this case are shown in Figure A1. The separation angle θ_s and separation shock angle β_s are all quite consistent with the results predicted by the MVD theorem [46].

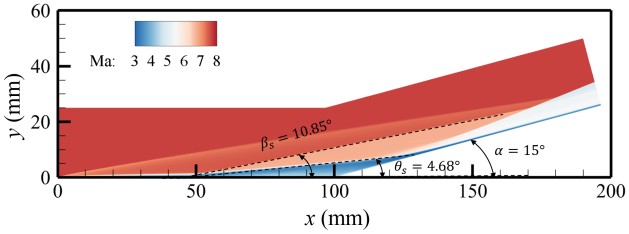
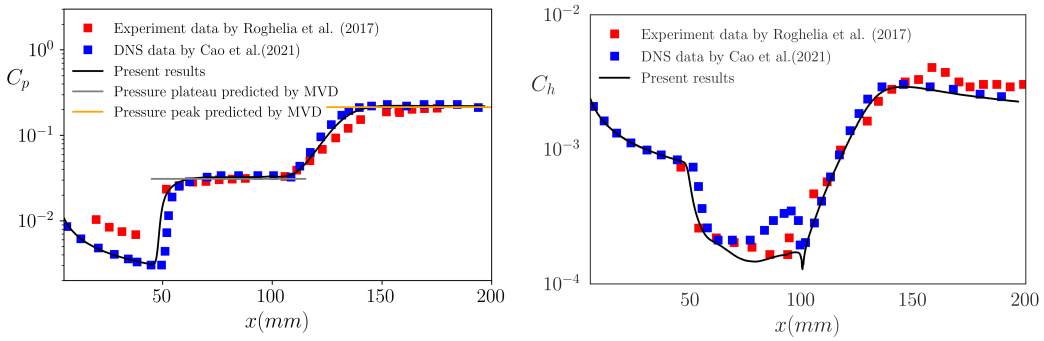


Figure A1. Mach number distributions with labeled separation angle θ_s and separation shock angle β_s predicted by MVD theorem.

Figure A2 compares the distributions of the pressure and Stanton number with experimental [55] and numerical results [56]. The distributions are in good agreement, including the separation length, the pressure plateau and pressure peak, as well as heat flux peak.



(a) **(b)**

Figure A2. A comparison of the numerical simulations with published experimental [55] and numerical results [56]. (**a**) Distributions of the pressure coefficient; (**b**) distributions of the Stanton number.

References

1. Simeonides, G.; Haase, W.; Manna, M. Experimental, Analytical, and Computational Methods Applied to Hypersonic Compression Ramp Flows. *AIAA J.* **1994**, *32*, 301–310. [CrossRef]
2. Simeonides, G.; Haase, W. Experimental and Computational Investigations of Hypersonic Flow about Compression Ramps. *J. Fluid Mech.* **1995**, *283*, 17–42. [CrossRef]
3. Babinsky, H.; Harvey, J. (Eds.) *Shock Wave-Boundary-Layer Interactions*; Cambridge Aerospace Series; Cambridge University Press: Cambridge, UK; New York, NY, USA, 2011.
4. Zhang, K. *Hypersonic Curved Compression Inlet and Its Inverse Design*; Advanced Topics in Science and Technology in China; Springer: Singapore, 2020; Volume 56. [CrossRef]
5. Silvester, T.B.; Morgan, R.G. Skin-Friction Measurements and Flow Establishment within a Long Duct at Superorbital Speeds. *AIAA J.* **2008**, *46*, 527–536. [CrossRef]
6. Dolling, D.S. Fifty Years of Shock-Wave/Boundary-Layer Interaction Research: What Next? *AIAA J.* **2001**, *39*, 1517–1531. [CrossRef]
7. Fukagata, K.; Iwamoto, K.; Kasagi, N. Contribution of Reynolds Stress Distribution to the Skin Friction in Wall-Bounded Flows. *Phys. Fluids* **2002**, *14*, 5. [CrossRef]
8. Gomez, T.; Flutet, V.; Sagaut, P. Contribution of Reynolds Stress Distribution to the Skin Friction in Compressible Turbulent Channel Flows. *Phys. Rev. E* **2009**, *79*, 035301. [CrossRef] [PubMed]
9. Renard, N.; Deck, S. A Theoretical Decomposition of Mean Skin Friction Generation into Physical Phenomena across the Boundary Layer. *J. Fluid Mech.* **2016**, *790*, 339–367. [CrossRef]
10. Li, W.; Fan, Y.; Modesti, D.; Cheng, C. Decomposition of the Mean Skin-Friction Drag in Compressible Turbulent Channel Flows. *J. Fluid Mech.* **2019**, *875*, 101–123. [CrossRef]
11. de Giovanetti, M.; Hwang, Y.; Choi, H. Skin-friction generation by attached eddies in turbulent channel flow. *J. Fluid Mech.* **2016**, *808*, 511–538. [CrossRef]
12. Shi, Y.; Xia, Z.; Chen, S. A new identification method in sampled quadrant analysis for wall-bounded turbulence. *Phys. Fluids* **2016**, *28*, 061702. [CrossRef]
13. Chan, C.; Örlü, R.; Schlatter, P.; Chin, R. Large-scale and small-scale contribution to the skin friction reduction in a modified turbulent boundary layer by a large-eddy break-up device. *Phys. Rev. Fluids* **2022**, *7*, 034601. [CrossRef]

14. Gatti, D.; Cimarelli, A.; Hasegawa, Y.; Frohnapfel, B.; Quadrio, M. Global Energy Fluxes in Turbulent Channels with Flow Control. *J. Fluid Mech.* **2018**, *857*, 345–373. [CrossRef]
15. Ji, Y.; Yao, J.; Hussain, F.; Chen, X. Vorticity Transports in Turbulent Channels under Large-Scale Control via Spanwise Wall Jet Forcing. *Phys. Fluids* **2021**, *33*, 095112. [CrossRef]
16. Chen, X.; Yao, J.; Hussain, F. Theoretical framework for energy flux analysis of channels under drag control. *Phys. Rev. Fluids* **2021**, *6*, 013902. [CrossRef]
17. Holden, M. Shock Wave-Turbulent Boundary Layer Interaction in Hypersonic Flow. In Proceedings of the 10th Aerospace Sciences Meeting, San Diego, CA, USA, 17–19 January 1972. [CrossRef]
18. Holden, M. A Study of Flow Separation in Regions of Shock Wave-Boundary Layer Interaction in Hypersonic Flow. In Proceedings of the 11th Fluid and Plasma Dynamics Conference, Seattle, WA, USA, 10–12 July 1978. [CrossRef]
19. Hung, F. Interference Heating Due to Shock Wave Impingement on Laminar Boundary Layers. In Proceedings of the 6th Fluid and PlasmaDynamics Conference, Palm Springs, CA, USA, 16–18 July 1973. [CrossRef]
20. Chang, E.W.K.; Chan, W.Y.; McIntyre, T.J.; Veeraragavan, A. Hypersonic Shock Impingement Studies on a Flat Plate: Flow Separation of Laminar Boundary Layers. *J. Fluid Mech.* **2022**, *951*, A19. [CrossRef]
21. Zhang, P.; Xia, Z. Contribution of Viscous Stress Work to Wall Heat Flux in Compressible Turbulent Channel Flows. *Phys. Rev. E* **2020**, *102*, 043107. [CrossRef]
22. Zhang, P.; Song, Y.; Xia, Z. Exact Mathematical Formulas for Wall-Heat Flux in Compressible Turbulent Channel Flows. *Acta Mech. Sin.* **2022**, *38*, 321403. [CrossRef]
23. Sun, D.; Guo, Q.; Yuan, X.; Zhang, H.; Li, C.; Liu, P. A Decomposition Formula for the Wall Heat Flux of a Compressible Boundary Layer. *Adv. Aerodyn.* **2021**, *3*, 33. [CrossRef]
24. Li, J.; Yu, M.; Sun, D.; Liu, P.; Yuan, X. Wall Heat Transfer in High-Enthalpy Hypersonic Turbulent Boundary Layers. *Phys. Fluids* **2022**, *34*, 085102. [CrossRef]
25. Wenzel, C.; Gibis, T.; Kloker, M. About the Influences of Compressibility, Heat Transfer and Pressure Gradients in Compressible Turbulent Boundary Layers. *J. Fluid Mech.* **2022**, *930*, A1. [CrossRef]
26. Agostini, L.; Leschziner, M. The Connection between the Spectrum of Turbulent Scales and the Skin-Friction Statistics in Channel Flow At. *J. Fluid Mech.* **2019**, *871*, 22–51. [CrossRef]
27. Sagaut, P.; Peet, Y. Theoretical Prediction of Turbulent Skin Friction on Geometrically Complex Surfaces. In *Progress in Wall Turbulence: Understanding and Modeling*; Stanislas, M., Jimenez, J., Marusic, I., Eds.; Springer: Dordrecht, The Netherlands, 2011; Volume 14, pp. 39–49. [CrossRef]
28. Bannier, A.; Garnier, É.; Sagaut, P. Riblet Flow Model Based on an Extended FIK Identity. *Flow Turbul. Combust.* **2015**, *95*, 351–376. [CrossRef]
29. Hu, Y.C.; Zhou, W.F.; Wang, G.; Yang, Y.G.; Tang, Z.G. Bistable States and Separation Hysteresis in Curved Compression Ramp Flows. *Phys. Fluids* **2020**, *32*, 113601. [CrossRef]
30. Hornung, H.G.; Oertel, H.; Sandeman, R.J. Transition to Mach reflexion of shock waves in steady and pseudosteady flow with and without relaxation. *J. Fluid Mech.* **1979**, *90*, 541–560. [CrossRef]
31. Chpoun, A.; Ben-Dor, G. Numerical confirmation of the hysteresis phenomenon in the regular to the Mach reflection transition in steady flows. *Shock Waves* **1995**, *5*, 199–203. [CrossRef]
32. Chpoun, A.; Passerel, D.; Li, H.; Ben-Dor, G. Reconsideration of Oblique Shock Wave Reflections in Steady Flows. Part 1. Experimental Investigation. *J. Fluid Mech.* **1995**, *301*, 19–35. [CrossRef]
33. Vuillon, J.; Zeitoun, D.; Ben-Dor, G. Reconsideration of Oblique Shock Wave Reflections in Steady Flows. Part 2. Numerical Investigation. *J. Fluid Mech.* **1995**, *301*, 37–50. [CrossRef]
34. Ivanov, M.S.; Ben-Dor, G.; Elperin, T. Flow-Mach-Number-Variation- Induced Hysteresis in Steady Shock Wave Re Ections. *AIAA J.* **2001**, *39*, 972–974. [CrossRef]
35. Hu, Y.C.; Zhou, W.F.; Tang, Z.G.; Yang, Y.G.; Qin, Z.H. Mechanism of Hysteresis in Shock Wave Reflection. *Phys. Rev. E* **2021**, *103*, 023103. [CrossRef]
36. Hu, Y.C.; Wang, G.; Zhou, W.F.; Tang, M.Z.; Yang, Y.G.; Tang, Z.G. The Bistability of Curved Compression Ramp Flows. *arXiv*, **2023**, arXiv:2304.03429.
37. Yang, Z.; Igarashi, H.; Martin, M.; Hu, H. An Experimental Investigation on Aerodynamic Hysteresis of a Low-Reynolds Number Airfoil. In Proceedings of the 46th AIAA Aerospace Sciences Meeting and Exhibit, Reno, Nevada, 7–10 January 2008. [CrossRef]
38. McCroskey, W.J. Unsteady airfoils. *Annu. Rev. Fluid Mech.* **1982**, *14*, 285–311. [CrossRef]
39. Mueller, T.J. The influence of laminar separation and transition on low Reynolds number airfoil hysteresis. *J. Aircr.* **1985**, *22*, 763–770.
40. Biber, K.; Zumwalt, G.W. Hysteresis Effects on Wind Tunnel Measurements of a Two-Element Airfoil. *AIAA J.* **1993**, *31*, 326–330.
41. Mittal, S.; Saxena, P. Prediction of Hysteresis Associated with the Static Stall of an Airfoil. *AIAA J.* **2000**, *38*, 933–935. [CrossRef]
42. Jin, Y.; Sun, S.; Tan, H.; Zhang, Y.; Huang, H. Flow Response Hysteresis of Throat Regulation Process of a Two-Dimensional Mixed-Compression Supersonic Inlet. *Chin. J. Aeronaut.* **2022**, *35*, 112–127. [CrossRef]
43. Zhou, W.F.; Hu, Y.C.; Tang, M.Z.; Wang, G.; Fang, M.; Yang, Y.G. Mechanism of Separation Hysteresis in Curved Compression Ramp. *Phys. Fluids* **2021**, *33*, 106108. [CrossRef]

44. Tang, M.Z.; Wang, G.; Xie, Z.X.; Zhou, W.F.; Hu, Y.C.; Yang, Y.G. Aerothermodynamic Characteristics of Hypersonic Curved Compression Ramp Flows with Bistable States. *Phys. Fluids* **2021**, *33*, 126106. [CrossRef]
45. Li, X.; Fu, D.; Ma, Y.; Liang, X. Direct numerical simulation of shock/turbulent boundary layer interaction in a supersonic compression ramp. *Sci. China Phys. Mech. Astron.* **2010**, *53*, 1651–1658.
46. Hu, Y.C.; Zhou, W.F.; Yang, Y.G.; Tang, Z.G. Prediction of plateau and peak of pressure in a compression ramp flow with large separation. *Phys. Fluids* **2020**, *32*, 101702.
47. Zhang, Z.; Tong, F.; Duan, J.; Li, X. Direct numerical simulation of supersonic turbulent expansion corner with shock impingement. *Phys. Fluids* **2021**, *33*, 105104.
48. Versteeg, H.K. *An Introduction to Computational Fluid Dynamics the Finite Volume Method, 2/E*; Pearson Education: London, UK, 2007.
49. Schlichting, H.; Gersten, K. *Boundary-Layer Theory*; Springer: Berlin/Heidelberg, Germany, 2017.
50. Xu, D.; Wang, J.; Chen, S. Skin-Friction and Heat-Transfer Decompositions in Hypersonic Transitional and Turbulent Boundary Layers. *J. Fluid Mech.* **2022**, *941*, A4. [CrossRef]
51. Noether, E. Invariante variationsprobleme. In *Gesammelte Abhandlungen-Collected Papers*; Springer: Berlin/Heidelberg, Germany, 1983; pp. 231–239.
52. Hanc, J.; Tuleja, S.; Hancova, M. Symmetries and conservation laws: Consequences of Noether's theorem. *Am. J. Phys.* **2004**, *72*, 428–435.
53. Halder, A.K.; Paliathanasis, A.; Leach, P.G. Noether's theorem and symmetry. *Symmetry* **2018**, *10*, 744. [CrossRef]
54. Duan, L.; Martin, M. Direct numerical simulation of hypersonic turbulent boundary layers. Part 4. Effect of high enthalpy. *J. Fluid Mech.* **2011**, *684*, 25–59.
55. Roghelia, A.; Olivier, H.; Egorov, I.; Chuvakhov, P. Experimental investigation of Görtler vortices in hypersonic ramp flows. *Exp. Fluids* **2017**, *58*, 1–15.
56. Cao, S.; Hao, J.; Klioutchnikov, I.; Olivier, H.; Wen, C.Y. Unsteady effects in a hypersonic compression ramp flow with laminar separation. *J. Fluid Mech.* **2021**, *912*, A3.

Disclaimer/Publisher's Note: The statements, opinions and data contained in all publications are solely those of the individual author(s) and contributor(s) and not of MDPI and/or the editor(s). MDPI and/or the editor(s) disclaim responsibility for any injury to people or property resulting from any ideas, methods, instructions or products referred to in the content.